Ash Sedimentation by Fingering and Sediment Thermals from Wind-Affected Volcanic Plumes

V. Freret-Lorgeril[1,*], J. Gilchrist[1,2], F. Donnadieu[1,3], A.M., Jellinek[2], J. Delanoë[4], T. Latchimy[3], J.P. Vinson[4], C. Caudoux[4], F. Peyrin[3], C. Hervier[3], S. Valade[5,+].

[1]*Université Clermont Auvergne, CNRS, IRD, OPGC, Laboratoire Magmas et Volcans, F-63000 Clermont-Ferrand, France*

[2]*Department of Earth, Ocean and Atmospheric Sciences, British Columbia University, Canada*

[3]*Université Clermont-Auvergne, CNRS, UMS 833, OPGC, F-63177 Aubière, France*

[4]*Laboratoire ATmosphère, Milieux, et Observations Spatiales (LATMOS), Guyancourt, France*

[5]*Dipartimento di Scienze della Terra, Università di Firenze, Firenze, Italy*

[*]*Department of Earth Sciences, University of Geneva, 13, Rue des Maraichers, CH-1205 Geneva, Switzerland*

[+] *GFZ German Research Centre for Geosciences, Telegrafenberg, 14473 Potsdam, Germany*

Corresponding author: valentin.freretlo@gmail.com

ABSTRACT

Ash fallout and volcanic plume dispersion represent critical hazards for local and global human populations for minutes to years after the onset of an eruption. Understanding the key processes governing the sedimentation of ash particles is a major challenge in modern volcanology from modelling and risk management perspectives. Recent experiments predict that sedimentation

from eruption clouds rich in fine-grained ash can be driven by convective phenomena in the form of ~100 m to km-scale ash fingers related to the intermittent formation and detaching of ash-rich particle boundary layer. Remote sensing observations of mammatus and cloud veils from numerous eruptions over recent years as well as field observations of spatially discontinuous ash deposits are consistent with this prediction. Indeed, this mode of ash sedimentation is predicted to be the predominant mechanism of fine ash removal for a significant fraction of eruptions in the geological records. Here, we use a novel combination of 3 millimeter-wavelength Doppler radar observations and time series of optical disdrometer data to characterize for the first time in real-time the time-varying structure and sedimentation properties of volcanic ash plumes under steady wind conditions. As a case study, we apply this new method to weak short-lived plumes from Stromboli Volcano. 96% of the disdrometer proximal sedimentation data highlight pulsatory phases of increased sedimentation rate that are 20-60 s apart and characterized by particle size distribution variation with bulk concentrations up to 681 mg/m^3. Radar data also record intermittent periods of higher reflectivity (*i.e.* a factor of 3 in mass concentration) inside the ash sedimentation interspersed by 30 to 50 s and interpreted as ash fingers crossing the radar beam. From time series of radar signals and ground-based disdrometer measurements, together with simple analog experiments, we develop a conceptual model for intermittent sedimentation from wind-affected ash plumes. In particular, we show that when wind speeds are comparable to or greater than ash settling velocities, the dynamics of wind-driven rolls in ash clouds can govern the production of gravitational instabilities and the occurrence and timing of ash fingers that form descending sediment thermals in turn. This study suggests that ambient wind should affect the maximum size and minimum concentration of ash particles needed to form fingers but also control where and when fingers form at the base of wind-drifted ash plumes. These novel predictions highlight the need

for future work aimed at refining our understanding of ash finger formation under windy conditions from the perspectives of in-situ characterization, numerical modelling and risk assessment of fine ash dispersal from the most frequent style of eruptions on Earth.

Highlights:

- Novel observations of time-dependent ash sedimentation using a 3 mm-wavelength Doppler radar and a ground-based disdrometer.
- Wind-induced counter-rotating rolls lead to the formation of ash fingers evolving into sediment thermals.
- Wind controls when and where ash fingers form at the base of wind-drifted ash plumes.

Keywords: volcanic plume; ash sedimentation; ash finger; sediment thermal; Doppler radar; optical disdrometer

1 Introduction

Ash plumes produced by explosive eruptions, such as the 2010 Eyjafjallajökull event, disrupt air travel and affect infrastructure and surrounding human populations (Horwell & Baxter, 2006; Tomašek *et al.*, 2016; Wilson *et al.*, 2012). Volcanic Ash Transport and Dispersion models (VATDMs) are used to forecast ash dispersal in the atmosphere and to predict impacted areas (Bonadonna *et al.*, 2011; Folch, 2012; Mastin *et al.*, 2009). VATDMs are initialized with the source parameters of an eruption, which include the Mass Eruption Rate (MER), plume heights, eruption duration, the Total Grain Size Distributions (TGSD) and the vent location. In addition, VATDMs are initialized using scenarios from past eruptions (Scollo *et al.*, 2009, 2010, 2013) or a calculation of mass load estimates from post-eruption deposit analyses (Bonadonna *et al.*, 1998; Bonadonna & Houghton, 2005; Bonadonna & Costa, 2012, 2013; Andronico *et al.*, 2014; and references therein). Although some models consider ash

density variations and aggregation processes (Costa *et al.*, 2010; Carazzo & Jellinek, 2012; Folch *et al.*, 2016), most of them assume ash settles via continuous individual particle settling, with progressively smaller particles settling out with increasing distance from the eruptive source (Pfeiffer *et al.*, 2005; Costa *et al.*, 2006; Folch, 2012; Bonadonna *et al.*, 2015). In these models, the TGSD, the ash concentration and, in turn, terminal settling velocity of ash particles control the description of ash sedimentation.

Many studies have shown that ash sedimentation from ash clouds can vary in space and time. For example, intermittent sedimentation, via ash fingers and mammatus, has been observed at Mount Saint Helens in 1980 (Hobbs *et al.*, 1991; Durant *et al.*, 2009; Carazzo & Jellinek, 2012), Soufrière Hills volcano in 1997 (Bonadonna *et al.*, 2002) and Eyjafjallajökull in 2010 (Manzella *et al.*, 2015). More generally, Carozzo & Jellinek (2012, Figure 8) show that the dynamics giving rise to fingers probably governed ash sedimentation in nearly half the deposits in geological record form which grain-size data is available. However, although analogue laboratory experiments and scaling theory constrain the conditions favoring the formation and evolution of ash fingers (Carazzo & Jellinek, 2012; Manzella *et al.*, 2015; Del Bello *et al.*, 2017; Scollo *et al.*, 2017), a critical knowledge gap is that their dynamics have not been characterized quantitatively *in situ.*

Accordingly, we use a novel 3 mm wavelength (95 GHz) Doppler radar together with an optical disdrometer to characterize volcanic cloud sedimentation dynamics during a series of eruptions at Stromboli in 2015, when the eruptive activity was mostly characterized by short-lived weak ash plumes (**Figure 1A**). Guided by time series radar data from this campaign, and qualitative observations of analog experiments, we propose that sedimentation through the production of ash-laden fingers evident in **Figure 1B** (Patrick *et al.*, 2007) at Stromboli, is a consequence of convective instabilities (*e.g.* Hoyal *et al.*, 1999; Bonadonna *et al.*, 2002; Bush

et al., 2003; Durant *et al.*, 2009; Carazzo & Jellinek, 2012, 2013; Manzella *et al.*, 2015; Scollo *et al.*, 2017) modified by wind effects including the production of wind counter-rotating rolls (Turner, 1960). We will argue that resulting overturning and stirring of the ash-air mixture enhances the production of Particle Boundary Layers (PBLs) and the formation of ash fingers. This class of time-dependent sedimentation also predicts deposits with spatially-varying textural characteristics that are readily identifiable in the field (Branney, 1991; Carazzo & Jellinek, 2012). Finally, our results suggest that finger formation is not only a common feature of sedimentation from transient and weak volcanic plumes, consistent with expectations from Carazzo & Jellinek (2012, figure 8), but also that their formation depends strongly on the character of wind-driven stirring.

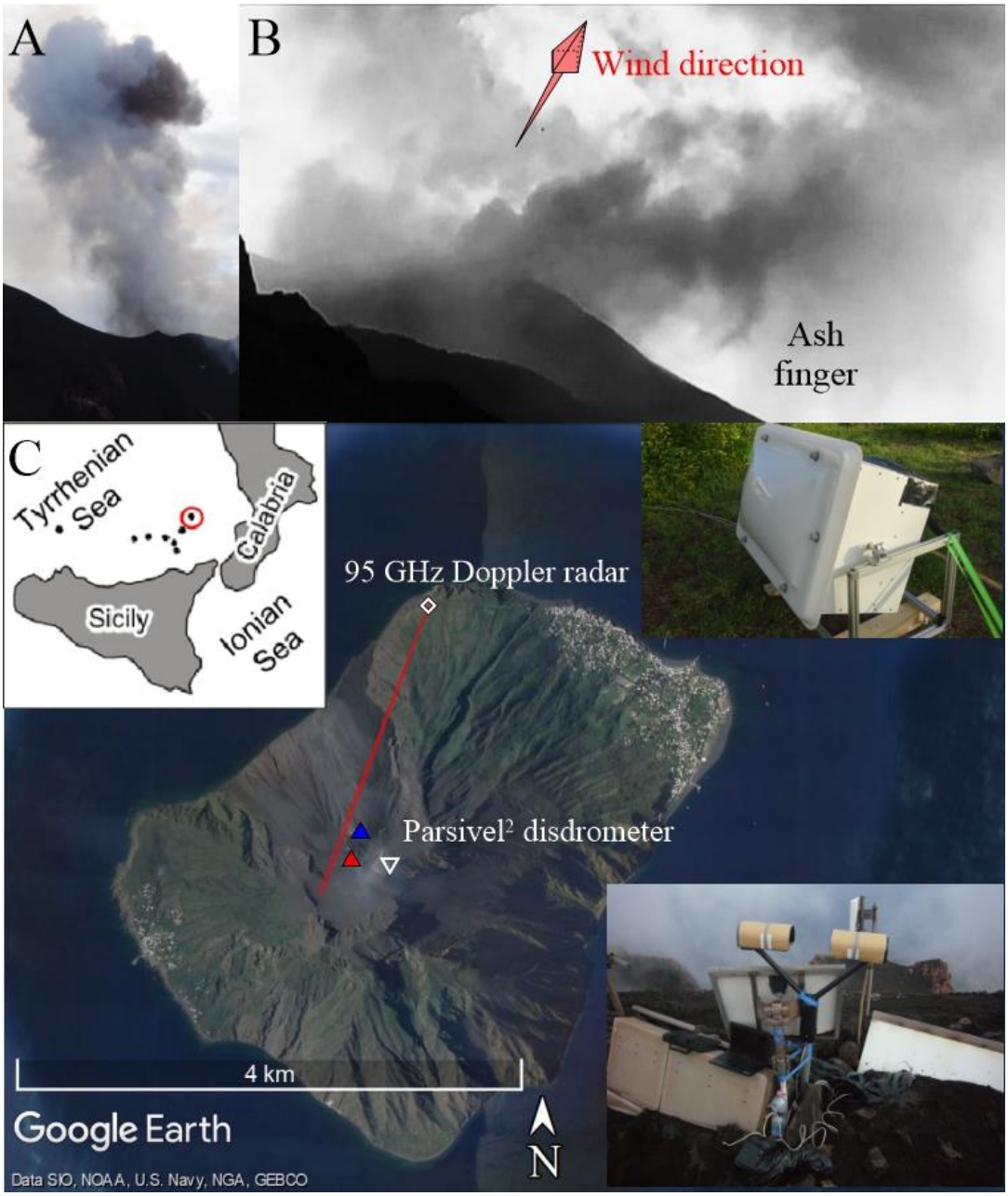

104

105 ***Figure 1**: **A)** Photograph of an ash plume emitted by the Southwest crater of Stromboli. **B)** Strombolian*
106 *ash plume drifted toward the North by the wind and forming an ash finger. The wind direction is shown*
107 *by the red arrow. **C)** Instrument setup at Stromboli Island. Upper right panel: 95 GHz radar at Punta*
108 *Labronzo (100 m a.s.l.) 2.1 km in slant distance from the vents (red line: radar beam direction). Lower*
109 *right panel: Disdrometer near Pizzo Sopra La Fossa at 900 m a.s.l., 350-450 m ESE of the summit*
110 *craters (SW crater, red triangle; NE Crater, blue triangle).*

Our paper is organized in the following way: in Section 2, we present the methodology we applied at Stromboli as a case study, between the 28th of September 2015 and the 4th of October 2015, for identifying and characterizing distinct sedimentation features of volcanic plumes. In section 3, we present the combined radar and disdrometer results and highlight principal observations. In section 4, we use observations and a small suite of analog experiments to build a conceptual model for intermittent sedimentation from weak volcanic plumes constrained by our principal observations before concluding in section 5.

2 Methodology

2.1 The measurement campaign at Stromboli

The goal of our measurement campaign is to characterize quantitatively the sedimentation behavior of volcanic plumes with three techniques: (i) a 3 mm wavelength Doppler radar (95 GHz), designed to track ash in volcanic plumes (**Figure 1C**); (ii) an optical disdrometer Parsivel^2 (**Figure 1C**); and (iii) analyses of ground deposit samples acquired during the campaign (Freret-Lorgeril *et al.*, 2019). In this study, it is important to note that each method detects a local Particle Size Distribution (PSD). Such size distributions represent only a part of the whole erupted mixture defined as the TGSD. From the disdrometer PSDs and phase delays in radar return, we determine the modal settling velocity of ash particles.

During 39 hours of monitoring, 181 short-lived ash plumes (*i.e.*, from type 2a and 2b explosions; Patrick *et al.*, 2007) were recorded by the radar and 26 sedimentation events by the optical disdrometer. The geometry of the instrument locations (**Figure 1C**), which was the same during the whole campaign, did not allow for simultaneous measurement of the same ash

sedimentation event as the wind was either blowing the sedimentation towards the radar or towards the disdrometer.

2.2 The optical disdrometer

The optical disdrometer Parsivel^2 designed by OTT HydroMet (**Figure 1C**) can measure particle settling velocities and diameter directly by converting the signal from a 780 nm wavelength laser beam, emitted from a transmitter to a receiver, into a voltage signal (**Figure 2A** and **2B**). The laser obscuration time is used to determine the settling velocity of falling particles, while the absorption amplitude, portion of the 54 cm^2 laser sheet surface obscured by the particle, measures the particle size (Löffler-Mang & Jürg, 2000; **Figure 2B**). Measurable settling velocity and size ranges are between 0.05-20.8 m/s and 0.250-26 mm. Disdrometers were originally designed for detecting hydrometeor precipitation. Nevertheless, Freret-Lorgeril *et al.* (2019) and Kozono *et al.* (2019) have highlighted the reliability of such instruments for detecting volcanic ash fallout with a high temporal resolution. Usually, disdrometer measurements are time-averaged either to avoid stochastic variations of measurements due to complex hydrometeor shapes (Löffer-Mang & Jürg, 2000) or to obtain stable quantitative data, e.g. rain-rates, for long-lasting meteorological events as opposed to short ash fallout events. Accordingly, we used the disdrometer maximum sampling frequency of 0.1 Hz (Tokay *et al.*, 2014) in order to capture short time-varying sedimentation processes.

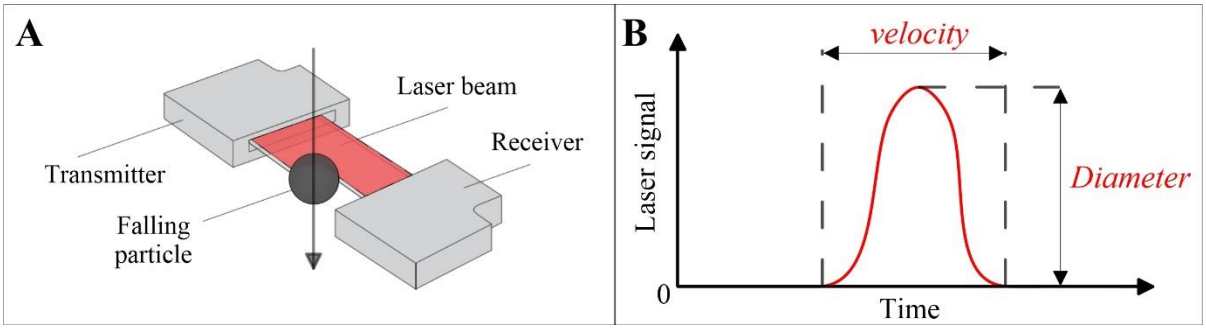

***Figure 2**: **A)** Sketch of the disdrometer detection procedure. A transmitter emits a laser sheet, i.e. in red, which is measured by a receiver. **B)** Signal of the laser as a function of time. The amplitude and time of the particle-induced laser obscuration are used to determine the size and the settling velocity of ash particles, respectively.*

Because of its lower detection limit and for accessibility reasons, the Parsivel^2 was set up next to Pizzo Sopra La Fossa at ~900 m a.s.l, 370 m NE of the SW crater (**Figure 1C**). This location allowed recording of the proximal coarse ash sedimentation. In addition, ground tarpaulins were placed next to the disdrometer to collect ash samples for each event recorded by the disdrometer. Freret-Lorgeril *et al.* (2019) demonstrated the influence of ash particle shape on disdrometer terminal settling velocity and size measurements. Since the disdrometer is designed to measure the shape of spherical droplets for meteorological applications, the shape of settling ash particles were constrained and determined with a morpho-grainsizer Morphologi G3® by Freret-Lorgeril *et al.* (2019). Assuming particles fall parallel to their shortest axis, the disdrometer detects particle with circle-equivalent diameter $D_{CE} \geq 0.230$ mm (Freret-Lorgeril *et al.*, 2019). The particle detection resolution (*i.e.* the disdrometer size classes) is equal to 0.115 mm in D_{CE}.

We calculate particle numbers over the range of measured particle D_{CE} and ash concentrations C_{ash} (kg/m^3) with (Freret-Lorgeril *et al.*, 2019):

$$C_{ash} = \frac{\pi \rho_{ash}}{6} \int_{D_{\min}}^{D_{\max}} N(D_{CE}) {D_{CE}}^3 dD_{CE} \,, \quad (1)$$

where $N(D_{CE})$ is the particle number density (m^{-3}/mm) of a size class crossing the beam, dD_{CE} (mm) is the diameter class width, and $\rho_{ash} = 2739 \pm 50$ kg/m^3 the average ash particle density measured by water pycnometry (Freret-Lorgeril *et al.*, 2019).

2.3 Radar observations of cloud structure and sedimentation

The 3 mm wavelength Doppler radar is a compact version of the prototype of Bistatic Radar System for Atmospheric Studies (BASTA, Delanoë *et al.*, 2016), using smaller antennas (30 cm wide). It was located at Punta Labronzo (**Figure 2A**), about 2 km NNE from Stromboli summit craters. We chose this location to capture plume emissions and their subsequent sedimentation that was preferentially dispersed towards the North due to ambient wind. The radar beam (0.8° wide) aimed at an area 100 m above the SW crater. Particle radial (along-beam) velocity components v_r and reflectivity factors Z are measured inside each probed volume of the beam as a function of time and range with resolutions of 2 s and 12.5 m (*i.e 12.5 m mode*), respectively (See **Table S1 in Supplemental information**).

Radial velocities $v_r < 0$ characterize particles with a motion component toward the radar, as expected for particles falling through the upward inclined beam (Sauvageot, 1992). The maximum non-ambiguous (*i.e* measurable by the radar without aliasing) velocity is ± 9.87 m/s (resolution of 0.01 m/s) in the 12.5 m mode used in this study. When detecting ash sedimentation, it is possible to estimate the settling velocity of detected particles V_T from their radial velocities. Under the assumption of no vertical component to the ambient wind, V_T can be estimated from the beam elevation angle (θ = 21.4°) and the range-time slope v_p of a sedimentation pattern crossing the radar beam. However, horizontal winds, which were present during the campaign, induce a velocity component along the radar beam axis and need to be deconvolved from the radar measurements. We were unable to obtain reliable wind data during the measurement campaign. Consequently, we exploit the radar beam geometry to constrain the average horizontal wind velocity, and in turn, a more accurate estimate of V_T.

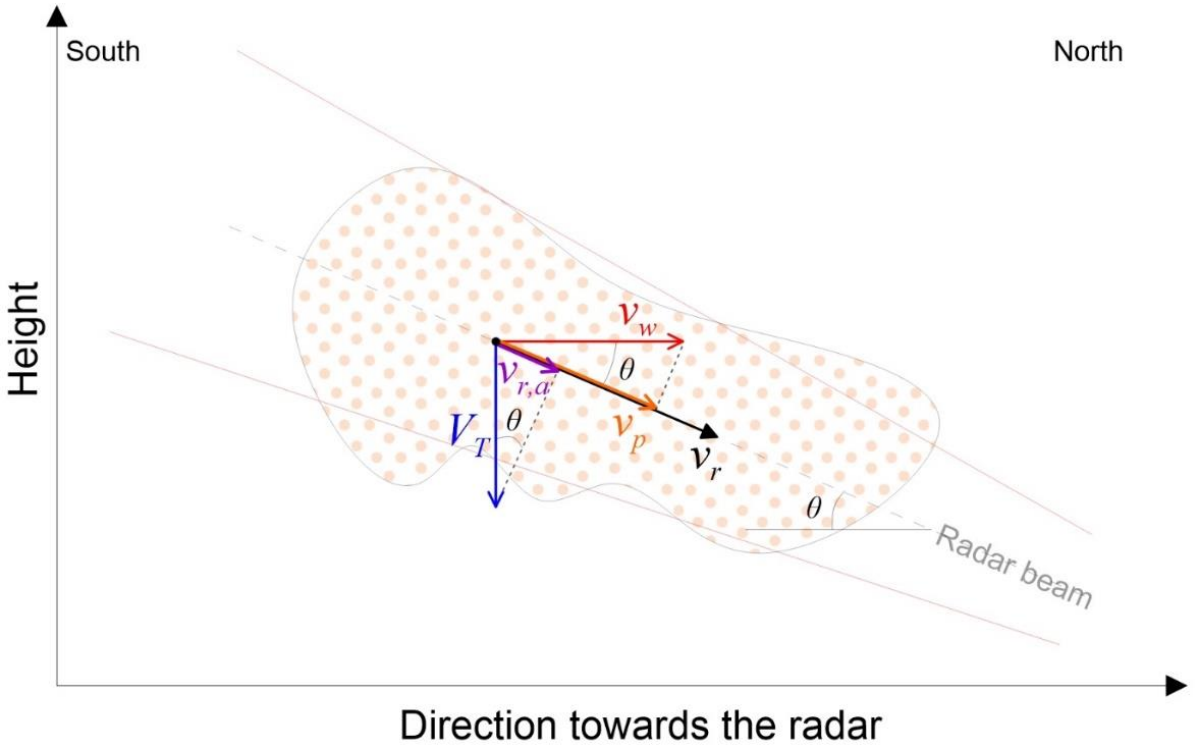

***Figure 3**: Schematic representation of measured and inferred velocity components of ash and wind, given a prescribed radar beam geometry. v_w is the horizontal wind velocity presumably inducing the along-beam (radial) displacement speed of the whole sedimentation pattern, v_p, measured from its range-time slope in reflectivity time series. v_r are the measured internal radial velocities of the recorded pattern. The measured differential velocity $v_{r,a} = |v_r| - |v_p|$, is assumed to be the radial velocity component related only to ash particles. The settling velocity V_T of particles in a sedimentation pattern is then calculated using **Equation 3**.*

Figure 3 shows each velocity component related to a sedimentation feature detected inside the radar beam. Under trigonometric considerations, the unknown horizontal wind velocity v_w, giving rise to the values of v_p, can be estimated with $|v_p|/\cos\theta$. Additionally, we can calculate the radial component velocity of the sedimentation, $v_{r,a}$, in the radar beam as:

$$v_{r,a} = |v_r| - |v_p|, \quad (2)$$

Finally, from the vertical component of $v_{r,a}$ the mean settling velocity of all the ash particles V_T is:

$$V_T = \frac{|v_r| - |v_p|}{\sin\theta} \quad . \tag{3}$$

Assuming that radar returns are in the Rayleigh scattering limit, the radar reflectivity factor, *Z*, characterizes the quantity of targets crossing the radar-beam and can also be calculated for the local PSD measured by the disdrometer, as (Sauvageot, 1992):

$$Z = \int_{D_{\min}}^{D_{\max}} N(D) D^6 dD \,, \tag{4}$$

where Z is in mm^6/m^3, $N(D)$ is the particle number density (mm^{-1}/m^3), D is the particle size in mm and dD is the range of particle size classes used (*e.g.* 0.115 mm resolution from disdrometer size classes). Z is expressed in logarithmic units (dBZ) as:

$$Z(\mathrm{dBZ}) = 10 \times \log_{10}(Z(\mathrm{mm}^6/\mathrm{m}^3)) \,. \tag{5}$$

Strictly, **Equations 4** are valid if we assume that the ash-air mixture is a dilute and homogeneous suspension of spherical particles with diameters less than about λ/4 (Gouhier & Donnadieu, 2008).

3 Results

3.1 Intermittent sedimentation from disdrometer records

We observed 24 sedimentation events in the optical disdrometer data associated with single ash plume emissions blown toward the instrument by an easterly wind. **Figure 4** shows a time series of five sedimentation events recorded by the disdrometer on October 3, 2015

between 12:35:02 and 14:50:02 UTC. These events, lasting between 110 and 340 s, are distinguished by time breaks during which no particles were detected. The multi-peaked variations in sedimentation rate, *i.e.* the mass of particle falling as a function of time and per unit area, shown for the five events in **Figure 4** are characteristic of 96% of the 24 events recorded by the disdrometer.

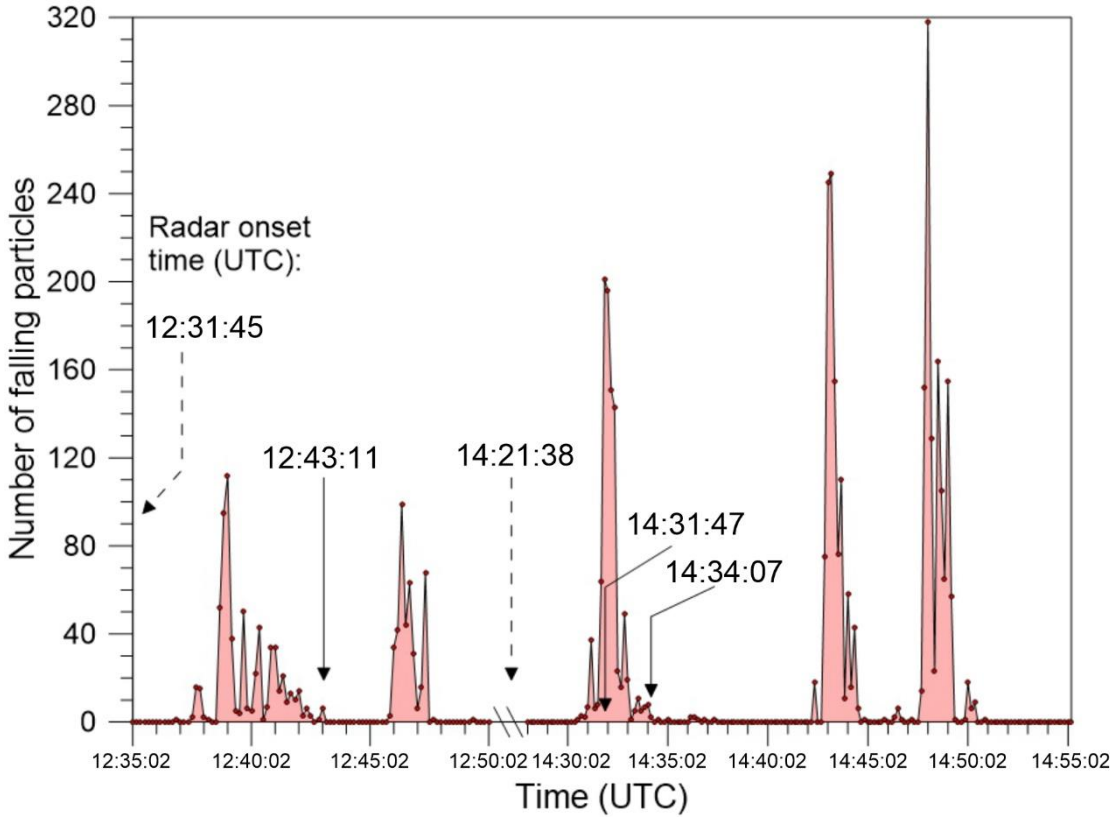

Figure 4: *Time series of the number of falling particles detected by the optical disdrometer on October 3, 2015 between 12:35:02-12:50:02 UTC and 14:25:02-14:50:02 UTC. The arrows show the first time that the radar detects the ash plumes rising above the vent, which occurs a few seconds after the start of each explosion. The ash sedimentation events are recorded several minutes afterwards.*

Figure 5 shows another 8 min-long sedimentation event comprised of 2,514 detected ash particles on October 3, 2015 between 09:49:00 and 09:59:00 UTC, originating from an ash plume emitted 7 minutes prior at 09:41:52 UTC. The PSD (**Figure 5A**) ranges from 0.230 <

D_{CE} < 0.690 mm (Class 1-4) and has a modal value between 0.345 and 0.460 mm (Class 2). Settling velocities (**Figure 5B**) range between 0.7 < V_T < 3.2 m/s with a modal value between 1.4 to 2 m/s. These are consistent with maximum settling velocities (cf., Ganser, 1993) of 1.8 < V_T < 2.4 m s^{-1} for Class 2 particles using a measured sphericity of 0.75 and average sizes between the longest and the intermediate axes of the particles (Freret-Lorgeril *et al.*, 2019). **Figure 5B** shows the widespread distribution of settling velocities as a function of particle size that is characteristic of all detected sedimentation events. In **Figure 5C**, the number of ash particles falling through the laser beam over time, and hence the sedimentation rate, shows significant fluctuations affecting all size classes. Six pulses of up to 145 particles occur with variations of 98% of the maximum pulse amplitude. The sedimentation can be divided into two main phases of 4 min 40 s and 3 min 10 s, respectively, that are separated by a 20 s interval with very few detected particles. Successive pulses within each sedimentation phase occur at intervals of 20 to 60 s and in between pulses, the sedimentation rate decreases for less than 10 s to one minute before increasing again.

Figure 5C shows expected radar reflectivity factor values derived from the sedimentation rate measured by the disdrometer using **Equations 4-5**. Z varies from -26.29 < Z < +12.85 dBZ for this event and, using **Equation 1,** we estimate average and maximum ash concentrations of 0.64×10^{-4} and 1.88×10^{-4} kg/m^3, respectively. For all sedimentation events observed in this study, the disdrometer data shows relatively constant PSD modes of 0.403 ± 0.058 mm comprising on average 46% of the total number of detected particles, ranging from 45 to 1,261. The ash concentrations inferred from Z values on the whole set of disdrometer data range between 7.61×10^{-7} to 6.81×10^{-4} kg/m^3.

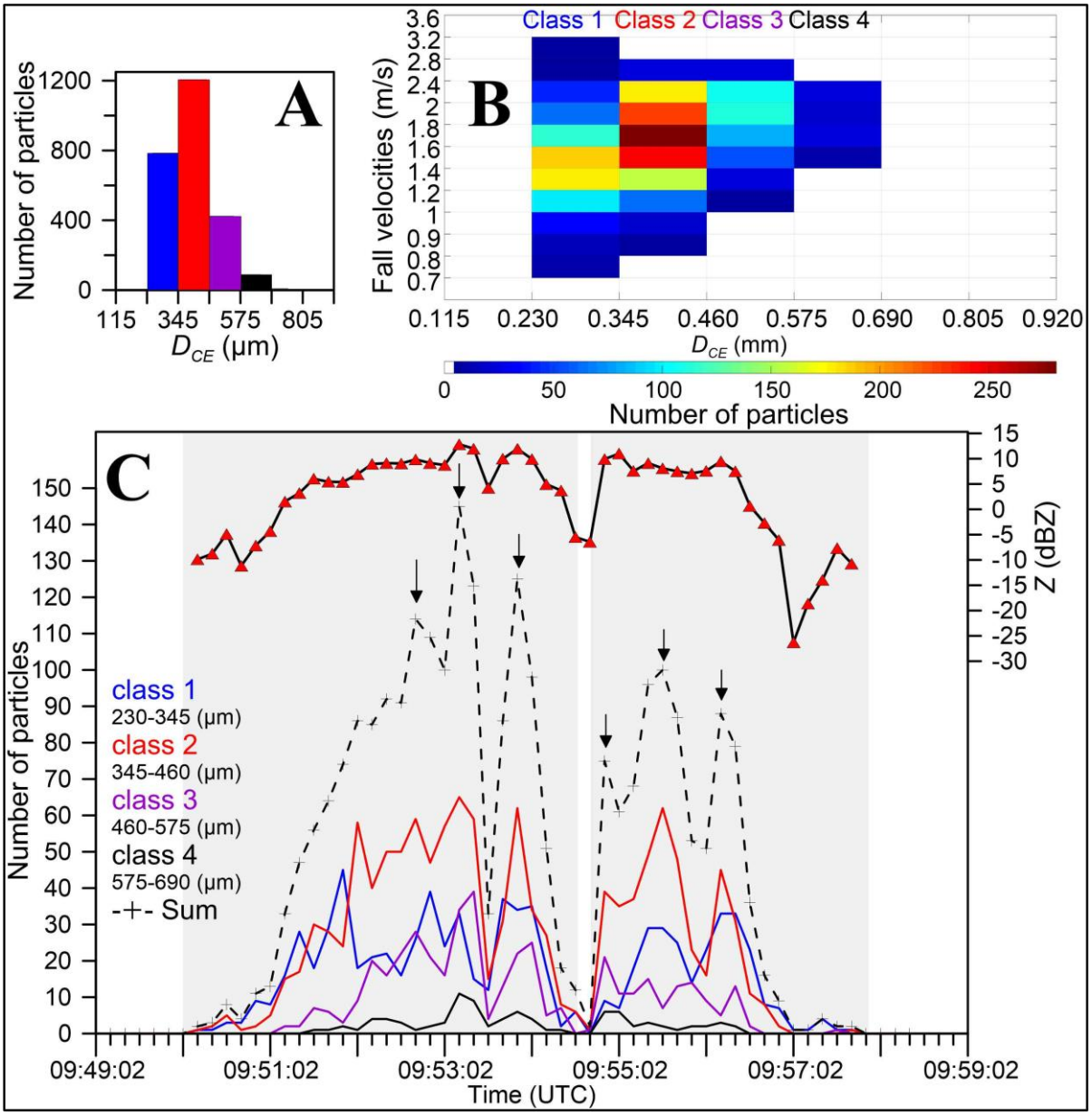

Figure 5: A) *Disdrometer-derived local Particle Size Distribution of the ash sedimentation event between 09:49:02 and 09:59:02 UTC on Oct. 3 2015. Each size class (± 0.05 mm) is color-coded.* ***B)*** *Settling velocities (V_T) measured by the disdrometer as a function of circle-equivalent diameters (D_{CE}). Bin colors represent number of particles.* ***C)*** *Temporal series of particle number of each class (colored lines), the total number of particles (dashed crossed line) and calculated reflectivity factor Z (red triangles). The grey areas and the black arrows represent the two sedimentation phases and the 6 sedimentation pulses, respectively.*

3.2. Radar observations of evolving cloud structure in space and time

Between October 2 and 3, 2015, weak northerly winds advected transient ash plumes towards the Doppler radar location at Punta Labronzo. The 3 mm wavelength Doppler radar detected the emission of ash plumes ~100 m above the vent and 15 subsequent ash sedimentation events over a ~2100 m slant distance. **Figure 6A** shows the range-time profiles of ash reflectivity factor, *Z*, with white arrows marking detected ash plumes rising above the vent at ~2000 m range. The first two detected ash plumes are followed by the detection of ash fallout, appearing as Long Duration Reflectivity Features (LDRFs) that grow in size as they move towards the radar site (white line in **Figure 6A**). The width of the first LDRF, detected at 15:23:00 UTC, is ~100 m until 15:29:00 UTC. During the following 3 min, it steadily widens to ~600 m. The second LDRF, detected at 15:47:00 UTC, steadily widens over the following 4 min from <100 m to ~200 m. For the remainder of the detection, its width thins and widens multiple times. The LDRFs do not appear to be homogeneous in *Z* along the radar beam axis and show small-scale range-time trends spaced quasi-periodically within their large-scale pattern (black arrows in **Figure 6A**). The slopes of the *small-scale reflectivity trends* are lower than the slope of the large-scale pattern.

The overall Doppler velocities, v_r, within the first LDRF show a decrease from ~0 m/s to ~-2 m/s around 15:26:00 UTC (**Figure 6B**). At about 15:28:00 UTC, the velocities vary spatially and intermittently above and below 0 m/s within the LDRF at later time and closer range. The second LDRF shows a similar evolution in v_r over time and range of detection.

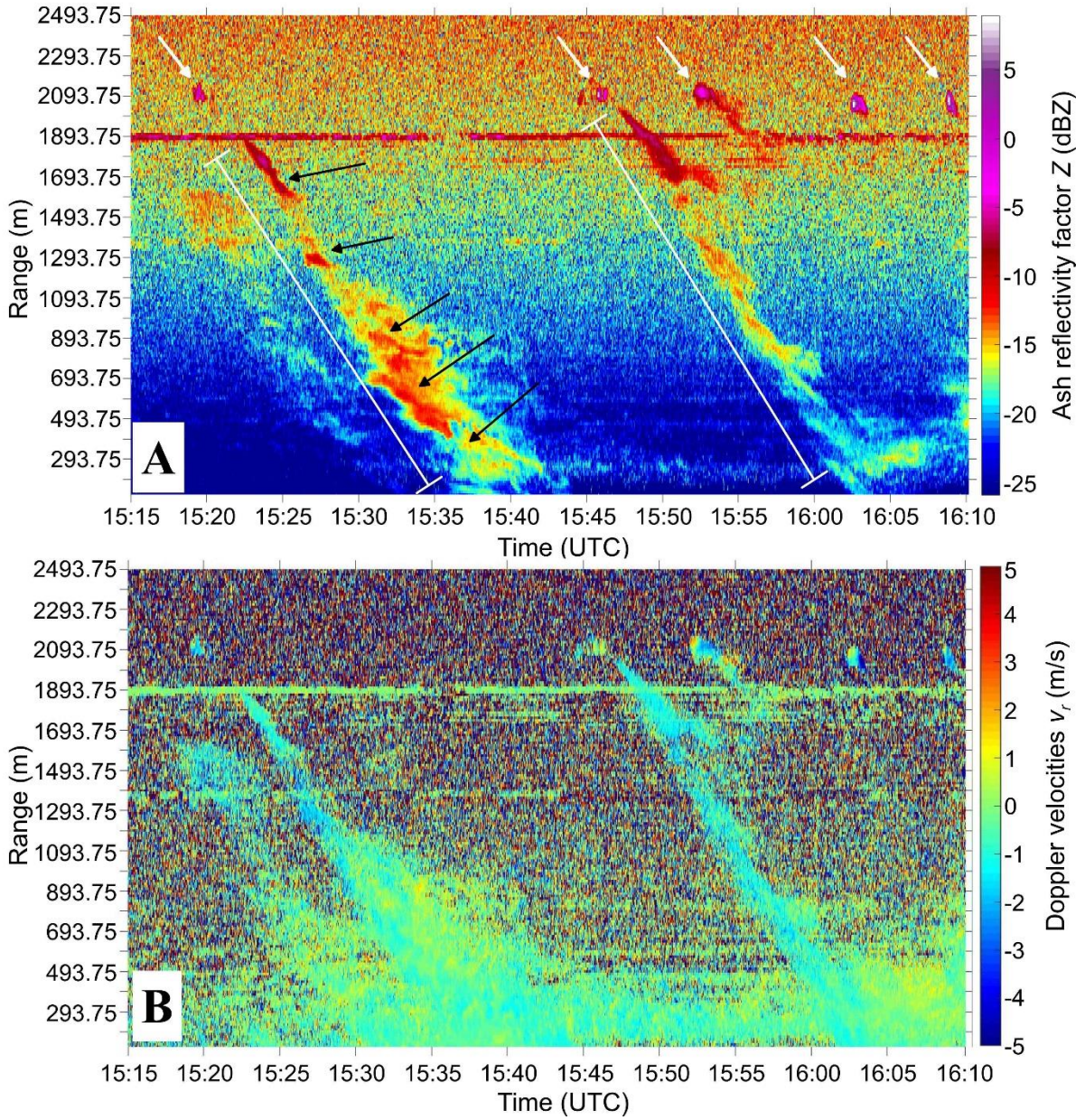

***Figure 6**: **A)** Ash reflectivity factor (Z) time series recorded on October 2 2015 (15:15-16:10 UTC) as a function of time (x-axis) and along-beam slant distance (y-axis: range). Five ash plumes are pointed by white arrows at crater distance (2100 m) while two Long Duration Reflectivity Features (LDRFs; indicated by white lines), lasting ~20 min each, are tracked over 2 km toward the radar location. Black arrows indicate example of small-scale range-time trends **B)** Range-time profiles of radial velocities of the same eruptions.*

In **Figure 7**, we show the sedimentation occurring within 1000 m of the SW Crater. The parent ash plume, which drifts to the north, is observed at slant distances of 2069-2119 m. As in **Figure 6A**, the range-time *Z* measurements show the ash plume rise, followed by a sedimentation event split into two phases. The first 20 s-long impulsive phase shows the ash plume detected 100 m above the vent at 14:26:44 UTC. Initially, it is < 50 m wide and then widens to 150 m in the N-S direction 16 s after detection (**Figure 7A**). 12 s after the detection onset, a maximum of 16.52 dBZ is reached in the bin at 2081 m. The following 158 s-long decrease in reflectivity until 14:29:42 UTC marks the ash plume exiting the radar beam. Radial velocities (v_r) in the emitted plume alternate in time between negative and positive values with a period of 24 s between the first and second yellow bands (see white arrows at top left in **Figure 7B**) and 40 s between the second and third yellow bands. The variations of the ash plume's internal velocities and reflectivity do not appear correlated.

After the initial ash plume exits the radar beam in **Figure 7**, there is a period of 123 s without ash detection. We detect ash again between 14:31:45 and 14:40:01 UTC at a lower altitude in downwind bins closer to the radar (994-1944 m) with a maximum reflectivity of Z_{max} = -4 dBZ, which is weaker than that of the initial ash plume. The width of this LDRF increases from 100 to 300 m from 14:33:30 to 14:34:45 UTC and its average slope indicates an average speed of -2.3 m/s towards the radar. Similar LDRFs, between 15:22:25-15:43:46 UTC and 15:47:02-16:08:09 UTC in **Figure 6A**, are detected within 2000 m of the radar location.

In **Figure 7**, three continuous features, with $-14.23 < Z < -4.72$ dBZ, emerge within the LDRF 160 s after its initial detection. These features are 25-100 m thick, 50 m on average and have range-time slopes that are distinct from the average slope of the overall LDRF signal. At 14:35:07 UTC, we observe three local maxima in *Z* values located in the middle of these features at different distances that have a relatively constant spacing of about 85 m (80 to 95

m) and intervals of 30 to 50 s (**Figures 7A** and **7C**). These small-scale reflectivity trends are best described by a constant along-beam slope, indicating a constant velocity component towards the radar. Thus, the reflectivity of the emitted ash plumes is characterized by an initial maximum decaying continuously, whereas the LDRFs detected closer to the radar are characterized by the emergence of multiple small-scale and evenly spaced reflectivity trends (**Figure 6A** and **Figure 7A**).

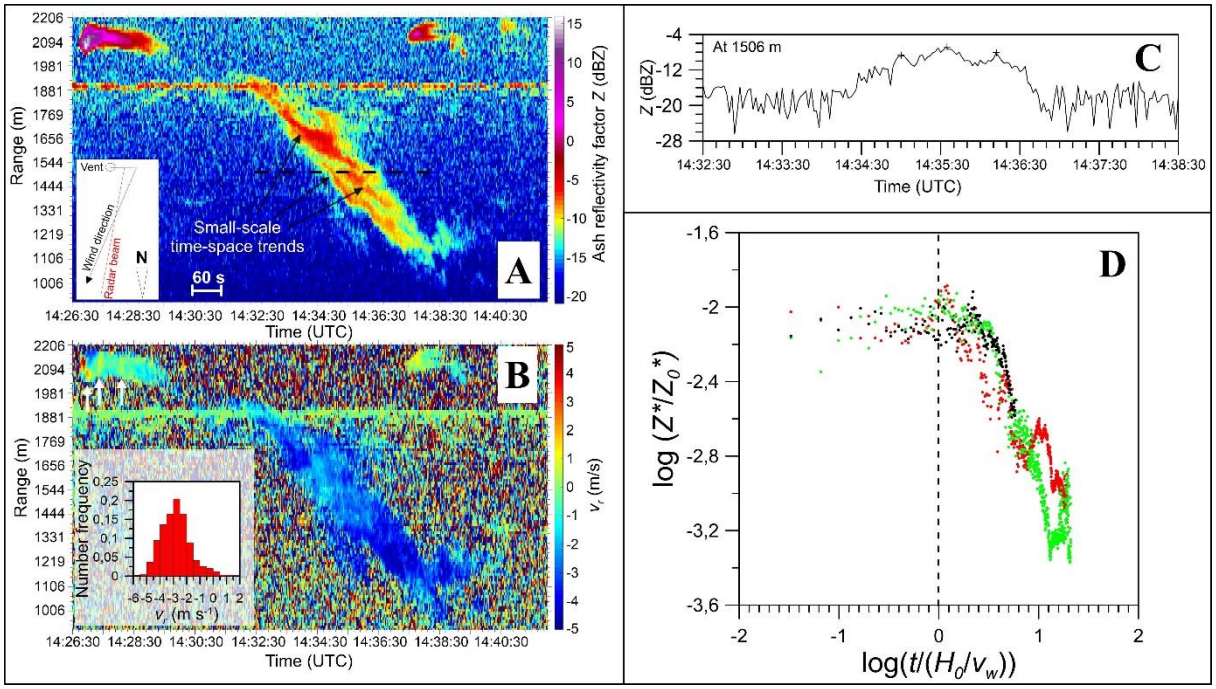

Figure 7**: **A)** Range-time profile of measured radar reflectivity factor, Z, of a single ash plume emission and subsequent LDRF. Red arrows indicate the small-scale reflectivity trends inside the LDRF. Inset: sketch of the wind direction according to the visually observed trajectory of the ash plume relative to the radar beam (at 2100 m and about 14:26 UTC on Oct. 2 2015). **B)** Range-time profiles of radial velocities of the same eruption. White arrows indicate the pattern of positive Doppler velocities in the emission. Inset: Histogram of Doppler (along-beam) velocities (filtered with threshold Z > -13 dBZ) inside the whole LDRF pattern. Doppler velocities mainly range between -5.5 to 1.5 m/s with a mode between -3 and -2.5 m/s. **C)** Z-profile across the three main small-scale range-time trends (peaks marked by crosses) at 1506 m from the radar between 14:32:30 and 14:38:30 UTC (black dashed line in **A**). **D)

Log-Log plot of the normalized reflectivity ratio (Z^*/Z_0^*) as a function of the normalized time scale for wind-driven overturning of rolls observed within the ash cloud $t/(H_0/v_w)$ (see text). Here, H_0 is the width of the parent plumes where the maximum reflectivity is detected in Figure 6 and 7A, and v_w is the horizontal wind velocity. The three events recorded by the radar on 2 October at 14:26 UTC (black dots), 15:17 UTC (green dots) and 15:44 UTC (red dots) show a decrease in normalized reflectivity factor.

In total, 93% of the Doppler velocities within the LDRF in **Figure 7** are marked by negative values within $-1 < v_r < -5$ m/s (inset in **Figure 7B**). They show an abrupt increase in overall v_r from ≤ -3 m/s to -0.7 m/s around 14:34:00 UTC and a return to ≤ -3 m/s closer to the radar around 14:36:30. The horizontal component of the LDRF's range-time slope in **Figure 7A** corresponds to a horizontal wind velocity, v_w = 2.47 m/s. From the LDRF's internal modal v_r, $-2.5 < v_r \leq -3$ m/s (inset in **Figure 7B**), a modal radial velocity $v_{r,a}$ between -0.2 and -0.7 m/s is found. The corresponding V_T ranges from 0.55 to 1.92 m/s (**Equation 3**), indicating detected particle sizes between 0.1 and 0.3 mm (Ganser, 1993; Freret-Lorgeril *et al.*, 2019).

A final observation was done on October 2, from 12:19 to 12:25 UTC, when LDRFs emerging in the radar data were accompanied by simultaneous visual observation of the formation of ash fingers under a dilute weak plume (**Figure 8**; **Supplemental information S2** and **video S2**). The same features observed in **Figures 6** and **7** are highlighted in **Figure 8**. Small-scale reflectivity trends are detected within a LDRF over a distance of 550 m (i.e. from 1256 m to 706 m along the radar beam) and during 284 s (**Figure 8**). The small-scale features show reflectivity ranging from -16 to -7 dBZ (**Figure 8A**). Finally, the LDRF is characterized by negative Doppler velocities alternating between -4 and -1 m/s (**Figure 8B**).

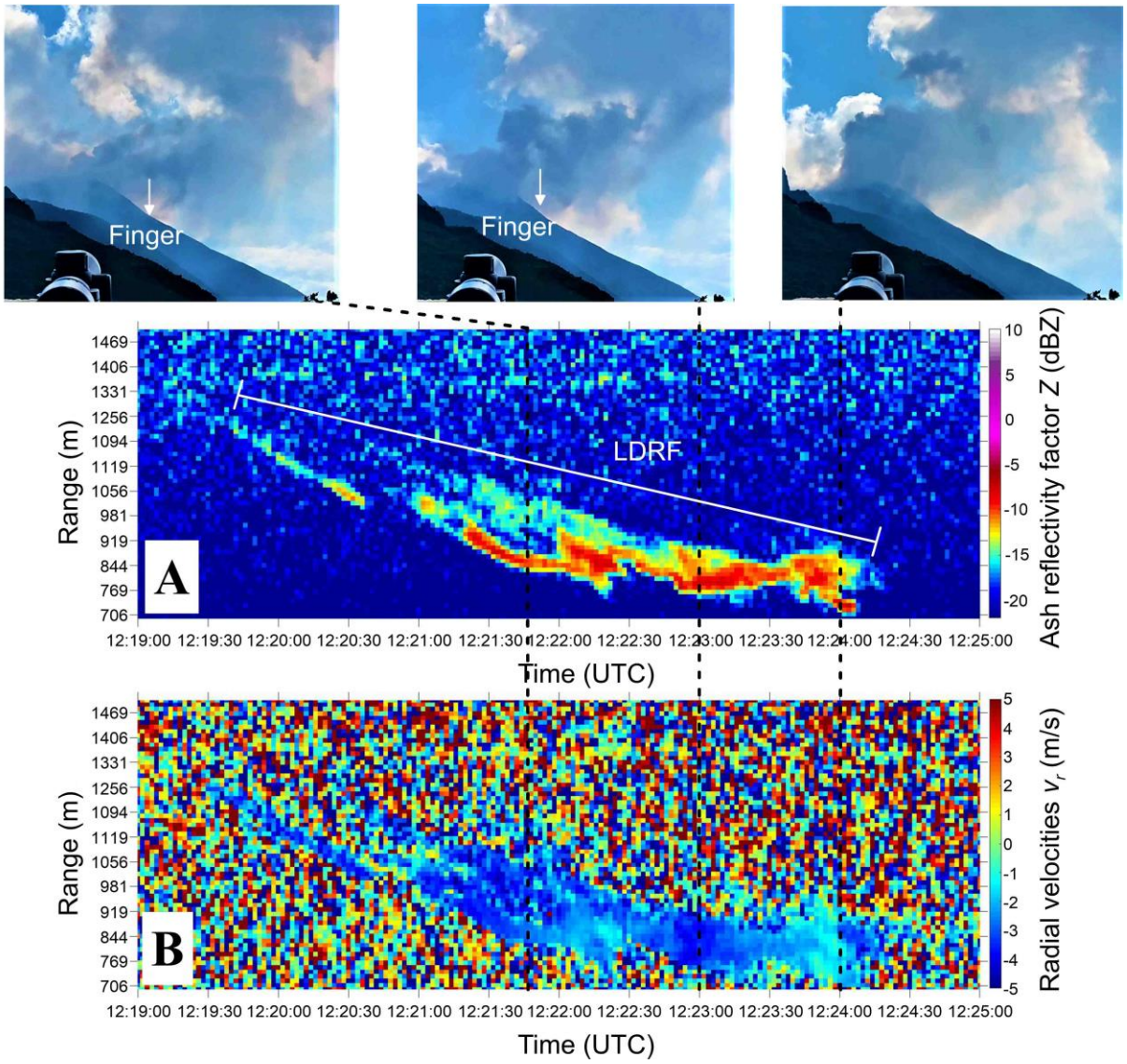

***Figure 8**: Simultaneous observation of ash fingering (black arrows) at Stromboli from visible (snapshots) and radar imagery on October 2, 2015 between 12:19 and 12:25 UTC. **A)** Range-time profile of ash reflectivity factor Z. The white dashed line indicates the detected LDRF. **B)** Range-time profile of radial velocities v_r.*

4 Discussion

The LDRFs detected by the radar over a range of 150 to 2000 m downwind from the vent (**Figures 6**, **7** and **8**) are interpreted as ash sedimentation from the October 2015 eruption

clouds. We interpret the temporal correlations between pulses in the sedimentation rate recorded proximally on the ground by the disdrometer (**Figures 4** and **5**) and the small-scale radar reflectivity trends (**Figures 6A** and **7A**) as evidence that the ash sedimentation is pulsed and quasi-periodic with recurrence intervals of 20-60 s in the disdrometer data and 30-50 s in the radar reflectivity data. On the basis of this consistency, the observations of finger-like structures in **Figure 1B**, **Figure 8** and the observations of ash curtains below Strombolian plumes in Patrick *et al.* (2007), we hypothesize that the sedimentation pulses are ash fingers arising from the same mechanism, which we now explore in detail.

4.1 A hypothesis for the origin, geometry and evolution of the ash fingers: Wind-driven rolls, convective fingering and sediment thermals

Before comparing the PSD measured by the disdrometer to that detected in the sedimentation targeted by the radar, several challenges must be addressed. First, the local PSD measured by the disdrometer only represents the fraction of the PSD falling at the location of the disdrometer (**Figure 2**). The largest pyroclastic particles are likely to fall out of the ash cloud before reaching the disdrometer. The disdrometer has also a lower detection limit of 0.230 mm and thus records a local PSD that is not only biased against the largest particles but also biased against fine ash, the dynamics of which probably control finger formation (Carazzo & Jellinek, 2012). Nevertheless, Freret-Lorgeril *et al.* (2019) have shown that the disdrometer local PSDs matched 75-94% (*i.e.*, in vol%) of the ground PSDs sampled at the same location. The total concentration measured by the disdrometer consequently sets a lower limit for the total ash concentration settling at its location. Additionally, transient non-dilute mixture effects such as enhanced or hindered settling (Del Bello *et al.*, 2017), potentially complicate V_T derived

389 from v_r. Bearing this in mind, we proceed with caution, to investigate the origin of the
390 sedimentation features.

391 Processes that drive the formation of fingers must explain four principal observations
392 from the combined disdrometer and radar data:

393 1. Quasi-periodic sedimentation pulses with wavelengths of 80-95 m and periods of 30-50 s
394 (**Figure 7A**).
395 2. An increase in size over time of the initial sedimentation pulses detected (**Figures 6A** and
396 **7A)**
397 3. The 120 - 360 s time scale for fingers to emerge (**Figure 6A** and **7A**) after initial detection
398 of ash sedimentation.
399 4. The overall increase of v_r within the sedimentation after 14:33:30 and 12:15:00 in **Figure**
400 **7B** and **Figure 8B**, respectively (after 15:28:00 for the first LDRF in **Figure 6B**).

401 Explosive volcanic eruptions, no matter their size and nature, are commonly
402 characterized by unsteady mass fluxes at the vent (Ripepe *et al.*, 1993; Donnadieu, 2012;
403 Scharff *et al.*, 2015; Chevalier & Donnadieu, 2015). If the source mass flux fluctuates
404 significantly over time, we would expect to see such fluctuations in the radar data acquired
405 above the vent. However, the reflectivity of the ascending ash plume detected by the radar
406 (**Figure 7A**) does not show such time-dependent behavior during the emission. Nonetheless,
407 the radar data do show an alternating pattern of positive and negative Doppler velocities (see
408 white arrows top left of this **Figure 7B**), which we interpret as internal motions within the
409 plume.

410 With an approximately constant mass eruption rate (at least over the time scale for
411 sediment fingers to form in our data), one mechanism for the quasi-periodic formation of the

fingers evident in **Figure 1B** and **Figure 8** is the intermittent growth and detachment of ash-rich particle boundary layers (Carazzo & Jellinek, 2012; Scollo *et al.*, 2017). If sufficiently strong, the wind will influence the timing of these convective effects in the Stromboli ash cloud in **Figure 1** and **Figure 8**. If we assume that the wind is horizontal, from the crater to the radar site, consistent with qualitative observations made in the field, we estimate the wind speed as the horizontal component of the overall range-time slope for the sedimentation in radar reflectivity data as v_w = 2.47 m/s (**Figure 7A**). This background wind is larger than the maximum inferred settling speeds for particles forming the median grain size in the PSD (**Figure 5C**) and will consequently affect their dynamics at leading order. For a cloud width H_0 (*i.e* where the maximum reflectivity is detected), wind-driven organization of the ash plume will occur over a time scale $t_w = H_0/v_w$. Because this time scale is comparable to or smaller than the time scale for particle settling $t_p = H_0/V_T$ for much of our inferred PSD, an initial prediction for particle buoyancy-driven sedimentation is that it will begin approximately at or shortly after ~1 t_w, which is consistent with **Figure 7D**. We consequently infer that there is strong particle-fluid coupling and these mixture buoyancy effects are more important than particle loss by their ejection from the rolls (i.e., so-called Stokes number effects). Moreover, if this inference is incorrect, the change in concentration in **Figure 7D** would begin at a different part of the evolution than where $t/(H_0/v_w) = 1$.

Although consistent with **Figure 7D**, this heuristic expectation provides little insight into the underlying mechanisms governing how particles become concentrated into mixtures sufficiently dense to form fingers (Carazzo & Jellinek, 2012). **Figure 7D** shows only that progressive particle loss occurs after ~1 t_w. Nonetheless, observations of fingers in the images of the wind-advected plume taken on October 2, 2015 (**Figure 1B**) indicate that the small-scale reflectivity trends in **Figure 6A** and **Figure 7A** represent ash fingers. If ash sedimentation is

436 only controlled by individual particle settling, we would expect to see an LDRF with no small-
437 scale reflectivity features within.

438 The maximum finger length, h_f below the parent ash cloud is $h_f = t_w V_f$, where V_f is the
439 finger fall velocity (see Equation 23 in Carazzo & Jellinek, 2012). If we assume that particle-
440 fluid mixtures forming fingers descend faster than individual particles (*i.e.*, a condition for
441 fingers to form in the first place) then we can take $V_f \approx V_T$ detected in the LDRFs in **Figure 7B**.
442 With H_0 = 100 m we find 189 < h_f < 300 m, in agreement with estimates from visual
443 observations of fingers in **Figure 1B** and **Figure 8**. Additionally, the initial increase in width
444 followed by a decrease in overall v_r of the LDRFs in **Figure 6A**, **Figure 7A** and **Figure 8B**
445 indicate that the volume of the fingers increases as they fall, which is followed by a decrease in
446 settling velocity soon after, consistent with the dynamics of sediment thermals (Bush *et al*.,
447 2003). On this basis, we propose that these are observations of fingers evolving into sediment
448 thermals (Ernst *et al.*, 1994; Bush *et al.*, 2003; Carazzo & Jellinek, 2012; Suzuki & Koyaguchi,
449 2013; Del Bello *et al*, 2017; Scollo *et al.*, 2017

450 *4.2 A conceptual model for the generation of fingers forming sediment thermals*

451 To build qualitative understanding of the sedimentation dynamics below wind-affected
452 volcanic plumes, we conduct simple experiments (described in the **Supplemental Information**
453 **S3**) in which we introduce dilute warm mixtures of 0.030, 0.190, 0.225 and 2 mm diameter
454 silica particles into water with an imposed constant crossflow velocity to form an advected
455 analog for the cloud shown in **Figure 1**. We choose ad hoc properties in the experiments to
456 capture the range in t_w/t_p inferred for our PSD for a wind speed of 2.47 m/s, and to explore
457 sensitivity of the cloud structure to this ratio of time scales (**Figure 9**). In **Figure 9A**, counter-
458 rotating rolls induced by the experimental crossflow develop along with regularly spaced

sedimentation features in the form of particle-laden fingers. They detach to form sediment thermals but retain the regular spacing of the features. Descending sediment thermals entrain ambient water and their buoyancy increases. This entrainment causes them to slow such that entrained particles sediment from their basal edges to form a second generation of smaller sediment thermals. The second generation of sediment thermals disperses and the dispersed clouds of both generations continue to settle to the tank floor at the terminal settling velocity of the modal particle size (0.03 m/s and 0.200 mm respectively) (Bush *et. al*, 2003; Carazzo & Jellinek, 2012).

Guided by the experimental observations from **Figure 9A**, previous studies (Ernst *et al*., 1994; Bush *et al.*, 2003; Carazzo & Jellinek, 2012; Scollo *et al*., 2017), and the field observations presented in this study we present the conceptual model. We key the main features of this model to 4 time slices (t_1-t_4 in **Figure 9B**), which indicate the sedimentation pulses in **Figure 7A** and those inferred in **Figure 9A**. The sketches of **Figure 9C** depict the formation of ash fingers over a time ~t_w evolving, in turn, into sediment thermals at the base of the volcanic ash cloud, as seen by the radar. The development of counter-rotating rolls in the particle cloud enhances the delivery of particles to its base, particularly where the flow in the rolls converge (Front view in **Figure 9C**). This relatively dense mixture undergoes gravitational instabilities to form fingers, in turn (Carazzo & Jellinek, 2012, 2013; Scollo *et al.*, 2017) (t_2 in **Figure 9C**; see also figures 3, 5, 6 and 9 in Scollo *et al.*, 2017). Fingers descend, entrain ambient fluid and decelerate (**Figure 9A**, t_3). This basic evolution agrees with the increase in cloud width (point 2 in section 4.1) and overall decrease of cloud settling velocity (point 4 in section 4.1) occurring simultaneously around 14:33:30. However, **Figure 7B** shows that the overall settling velocity increases after 14:36:30, which could imply that a second generation of sediment thermals has formed, similar to that observed at t_4 in the **Figure 9A**.

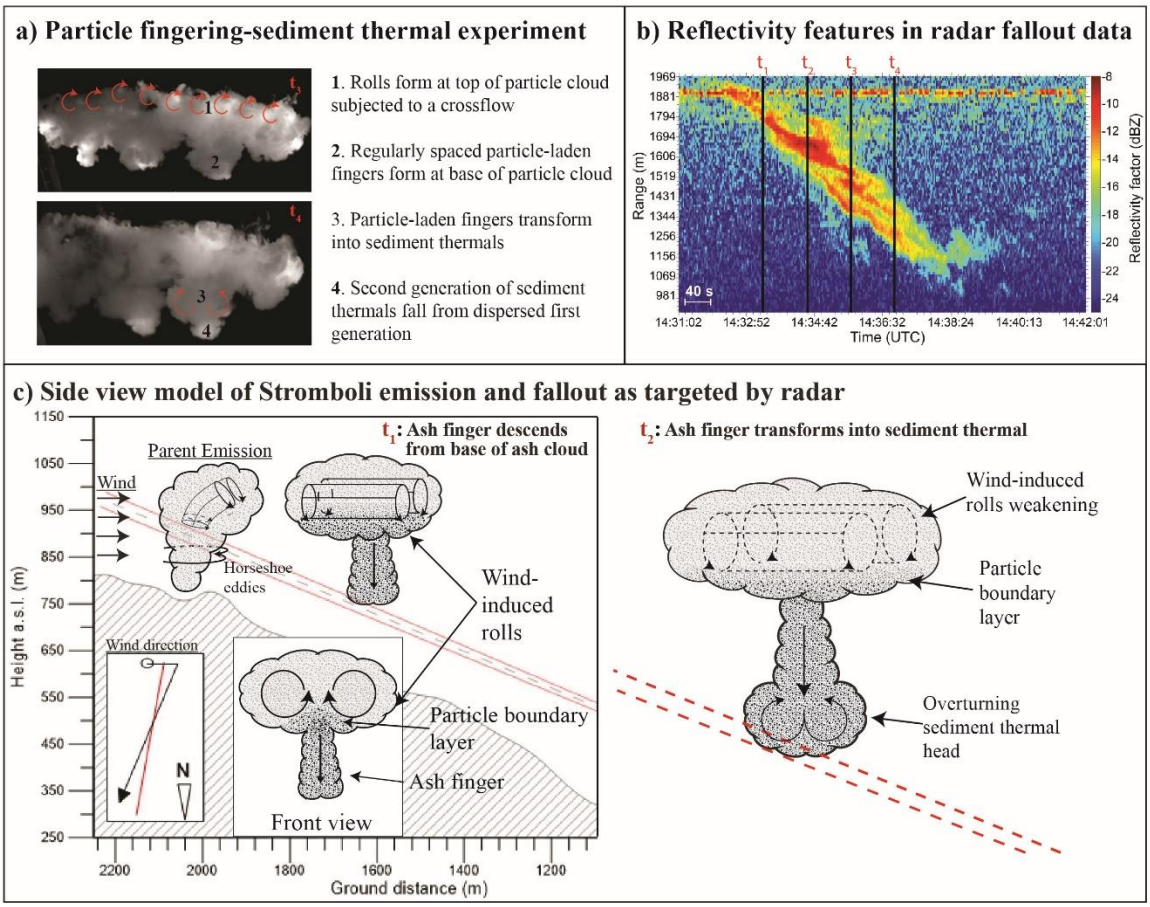

483

484 ***Figure 9*: *A)*** *Photo of polydisperse particle cloud experiment exhibiting regularly spaced particle-laden*
485 *fingers transforming into sediment thermals. Crossflow is from left to right, nearside counter-rotating*
486 *roll indicated by number 1 with red arrows showing fluid motion and sediment thermals are marked by*
487 *numbers 2 and 3 with red arrows showing overturning head fluid motion.* t_4 *corresponds to instance in*
488 *A), which represents the second generation of sediment thermals.* ***B)*** *Zoomed view of sedimentation*
489 *pulses in* ***Figure 7A*** *with black bars representing four instances in time* (t_1-t_4). ***C)*** *Model sketches of*
490 *parent ash emission with crosswind generating horseshoe eddies that induce counter-rotating rolls in*
491 *resulting ash cloud.* t_1 *and* t_2 *show sedimentation behavior at instances in time corresponding to* t_1 *and*
492 t_2 *in A), with radar beam in red.* t_1 *shows side and front views of ash cloud with arrows indicating flow*
493 *direction for counter-rotating rolls and initial finger instability. Darker particles at base of ash cloud*
494 *in Front View and* t_2 *highlight the Particle Boundary Layer formation enhanced by counter-rotating*
495 *rolls above.* t_2 *shows overturning motions at head of finger as it evolves into a sediment thermal (Ernst*

et al., 1994; Bush et. al, 2003; Carazzo & Jellinek, 2012, 2013; Suzuki & Koyaguchi, 2013; Del Bello et al., 2016; Scollo et al., 2017).

Predictions from the conceptual model in **Figure 9** satisfy the list of observations we identify in section 4.1 and make additional predictions, in line with our observations:

1. Fingers transitioning into sediment thermals: Periodic structure of the sedimentation pulses in space and time (**Figures 4**, **5**, **6**, **7** and **9**).
2. Entrainment and finger/thermal dilution: The volumetric growth of sediment thermals through entrainment is consistent with observed increases in size in **Figures 6** and **7A**, and the decrease in reflectivity density of the initially detected sedimentation pulses in **Figure 7D**. Dilution through entrainment is also consistent with the overall increase of v_r within the sedimentation, indicating a decrease in settling velocity, occurring after 14:34:30 in **Figure 7B** and after 12:22:00 and 12:23:30 in **Figure 8B**, respectively.
3. Multiple generations: The entrance of later forming fingers into the radar beam, after the initial finger enters the radar beam, explains the emergence of periodic sedimentation structure after the first sedimentation pulse is detected (**Figure 7A**). In particular, the particle loading supplied by a second generation of sediment thermals may explain the curious decrease of v_r (between 15:26:00 and 15:28:00 in **Figure 6B**; after 14:36:30 in **Figure 7B**), which indicates an increase in settling velocity, later in the sedimentation.
4. Sediment thermals, entrainment and individual particle settling: The dispersal of sediment thermals leads to individual particle settling, which is captured by the radar and can explain the modal v_r in the sedimentation corresponding to a smaller size range of particles than that detected by the disdrometer. The faster fall velocity of sediment

thermal mixtures *vs* the terminal settling velocity of the particles that compose them can explain the extreme values of v_r, ≤ -3 m/s detected in the sedimentation (**Figure 7B**).

5. Theoretical plausibility of sediment fingers: The modal value of the local PSD measured at the disdrometer (0.345-0.460 mm) and the modal value derived from v_r (0.100-0.300 mm) are both consistent with theoretical constraints indicating a 0.060-0.250 mm particle size limit for the formation of fingers for plausible ash concentrations (Carazzo & Jellinek, 2012, Figure 8). Moreover, the maximum ash concentration derived from the disdrometer measurements, 0.681 g/m^3, is comparable to the minimum concentration required (1 g m^{-3}) for the development of gravitational instabilities determined from scaling arguments. (Carazzo & Jellinek, 2012; Manzella *et al.*, 2015). Furthermore, radar measurements of ash cloud thickness, finger fall and ambient wind velocity predict a finger length, $189 < h_f < 300$ m, which is consistent with the observations in **Figure 1B**.

4.3 Wind-affected ash finger sedimentation

Ash fingering requires the formation of PBLs, which are expected to govern ash sedimentation in highly explosive eruptions (Carazzo & Jellinek, 2012), as well as the relatively weak events at Stromboli in 2015 (*i.e.*, type 2 explosions of Patrick *et al.*, 2007; **section 2.1**). It is important to note that the ash clouds observed in this study are not related to large MERs or high concentrations of particles, *i.e.* two mandatory conditions for the formation of gravitational instabilities in addition to the presence of fine ash, after Scollo *et al.*, 2017. Hence, our new finding at Stromboli that will enter in consideration for how and when ash fingers form generally is that wind-driven stirring can modulate the growth and timing of PBLs. In particular, unsteady wind-driven motions can form spatially local zones of fine-grained ash concentration where counter-rotating vortices meet (**section 4.2**). We expect the occurrence of these wind effects on sedimentation to be common features of any ash cloud for which $t_w \sim t_p$ (**section 4.1**).

Furthermore, these effects will be enhanced in clouds with higher particle concentration and a greater proclivity for PBL formation (Carazzo & Jellinek, 2012).

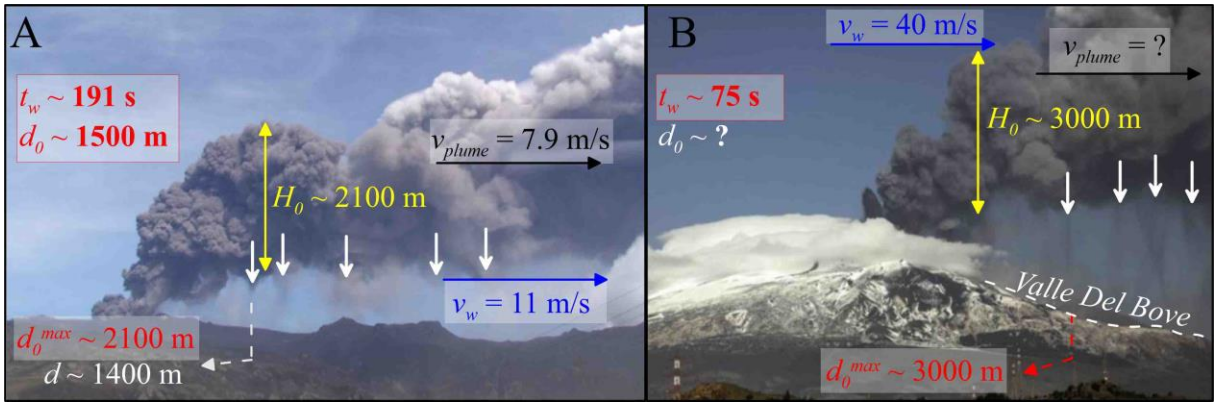

Figure 10: *Ash plume snapshots of* ***A)*** *the Eyjafjallajökull long-lasting plume on 4 May 2010 (figure modified from Manzella et al., 2015) and* ***B)*** *the 23 November 2013 paroxysmal tephra plume at Mount Etna (Figure modified from Scollo et al., 2017, source: www.tboeckel.de/EFSF/efsf_etna/Etna2013/Etna_11_13/volcano_etna_11_2013_e.htm). White arrows indicate ash finger location. Are reported on both figures the horizontal plume and wind speed (v_{plume} and v_w), the plume width (H_0), the distance from the vent where the first finger is observed (d) or is expected due to wind-driven organization (d_0) and the maximum distance d_0^{max} assuming v_w=v_{plume}.*

However, among the studies relating to ash finger formation (Carazzo & Jellinek, 2012, 2013; Manzella *et al.*, 2016; Scollo *et al.*, 2017; and reference therein), the potential for wind-driven dynamics of ash finger sedimentation and potential impact on ground in a natural system have only been explored by Manzella *et al.* (2015) during the Eyjafjallajökull eruption in 2010. This study provides detailed observations of a long-lasting plume emitted on 4 May 2010. The plume horizontal velocity v_{plume} was ~7.9 m/s with a horizontal v_w at its base of 11 m/s (**Figure 10A**). Considering a plume width H_0 of ~2100 m obtained from **Figure 10A**, we derive a wind-driven organization time (see **section 4.1**) t_w of 191 s. This value, multiplied by v_{plume}, leads to a distance d_0 of ~1500 m being similar to the ~1400 m from which fingers are continuously

observed (Manzella *et al.*, 2015). Therefore, our results for transient weak Strombolian plumes help to reconcile key observations of sedimentation from the relatively continuous Ejyafjallajökull event: Fingers appear approximatively or shortly after ~1 wind-driven organization time t_w. Also, if we take $v_{plume}=v_w$, we obtain a maximum distance at which the first finger should form with d_0^{max}= 2100 m, approximately the width of the plume. Hence, evidence of ash fingers on ground deposit should emerge at a distance greater than d_0^{max}, depending on the horizontal speeds of the fingers and their settling velocity (Manzella *et al.*, 2015).

We have applied the same reasoning for a weak plume emitted during the 23 November 2013 paroxysm at Mount Etna (**Figure 10B**). For this eruption, less information (*e.g.* distance of finger formation and plume horizontal speed) is available except for a wind speed of ~40 m/s and a plume width of ~3000 m (Corradini *et al.*, 2016; Montopoli, 2016). Considering the maximum plume velocity to be equal to v_w leads to d_0^{max}=3000 m. Although less precise than the previous calculation for Ejyafjallajökull, this simple estimate seems reasonable at Etna regarding the visually observed location of the first fingers inside La Valle del Bove from **Figure 10B**.

Predictions based on our observations and conceptual model constitute a step forward in understanding the location, timing and overall character of ash sedimentation driven by wind-affected PBL convective dynamics. Nevertheless, quantitative observations of ash finger formation remain poorly constrained for most eruptive events. Future field observations should include high space-time resolution instruments similar to our Doppler radar to more precisely constrain ash finger dynamics from transient and weak volcanic plumes *in situ*. Finally, given the major control of wind on the 3-dimensional structure and dynamics of PBLs, future

585 experiments should address finger formation in the presence of background wind velocity fields
586 with varying strength and direction.

587 **5 Conclusions**

588 Quantifying the processes leading to ash finger formation *in situ* is a key challenge to
589 understand their impacts on ground deposits and how fine ash is dispersed in the atmosphere.
590 Our joint radar-disdrometer study aims to characterize, quantitatively, the behavior of
591 heterogeneous ash sedimentation from volcanic plumes at high spatial and temporal resolution.
592 As a case study, the campaign carried out at Stromboli in 2015 demonstrates an effective
593 approach for monitoring volcanic ash plumes and for characterizing the internal dynamics of
594 their sedimentation.

595 Our observations of ash sedimentation show that ash sedimentation is time dependent,
596 potentially periodic, and well explained as a consequence of wind-affected gravitational
597 instabilities to ash-air mixtures in the form of ash fingers. Our results support a hypothesis that
598 wind-induced counter-rotating rolls may concentrate ash particles such that the formation and
599 release of relatively dense ash-air mixtures occurs over a time scale that is small in comparison
600 to individual particle settling.

601 In more detail, we have provided evidence that the maximum particle size and minimum
602 concentration favoring fingering dynamics at the base of volcanic plumes (Carazzo & Jellinek,
603 2012, Scollo *et al.*, 2017) may be influenced by ambient wind. Estimates of the *in-situ* ash size
604 distribution and concentration across the fingers are, however, required for a more thorough
605 comparison of these data with existing theoretical constraints on the basis of laboratory
606 experiments. Time-dependent wind-induced counter-rotating rolls in ash plumes are not a new
607 phenomenon and have been observed for a wide spectrum of eruptive activity (Ernst *et al.*,

1994; Suzuki & Koyaguchi, 2013). However, their role in ash finger formation was not previously quantified. Accordingly, we show that ash fingers may form approximatively at or shortly after one wind-driven organization time. Finally, if counter-rotating rolls, fingering and sediment thermal dynamics emerge even for very dilute and short-lived ash plumes observed in this study, we expect these physical processes to be common features of wind-affected explosive volcanic plumes with higher fine ash concentrations that have a greater proclivity for particle boundary layer-related dynamics to occur (Carazzo & Jellinek, 2012). Our newly proposed model for the effect of wind on ash finger formation can be tested with future experimental studies and may need to be parameterized for ash cloud dispersal and fallout modelling in the framework of ash hazard assessment following explosive eruptions.

ACKNOWLEDGMENTS

We acknowledge DPC members for their invaluable help at Stromboli, M. Ripepe (Univ. Firenze) and the Mayor of Lipari for facilitating our work. All OPGC colleagues are deeply acknowledged for their work and enthusiasm in the field. We also thank three anonymous reviewers whose comments helped to improve significantly the manuscript. This research was financed by the French Government Laboratory of Excellence initiative n°ANR-10-LABX-0006 (ClerVolc contribution number XX) and by TerMEx-Mistrals INSU-CNRS program. A.M. Jellinek and J. Gilchrist were supported by an MSERC Discovery grant to A.M. Jellinek.

REFERENCES CITED

Andronico, D., Scollo, S., Cristaldi, A., Lo Castro, M. D., 2014. Representivity of incompletely sampled fall deposits in estimating eruption source parameters: a test using the 12-13 January 2011 lava fountain deposit from Mt. Etna volcano, Italy. Bull. Volcanol. 76(10):861, doi:10.1007/s00445-014-0861-3.

631 Bonadonna, C., Houghton, B.F., 2005. Total grain-size distribution and volume of tephra-fall
632 deposits. Bull. Volcanol. 67, 441–456, doi:10.1007/s00445-004-0386-2.
633 Bonadonna, C., Ernst, G. G. J., Sparks, R. S. J., 1998. Thickness variations and volume
634 estimates of tephra fall deposits: the importance of particle Reynolds number. J. Volcanol.
635 Geotherm. Res. 81, 173–187.
636 Bonadonna, C., Macedonio, G., Sparks, R.S.J., 2002. Numerical modeling of tephra fallout
637 associated with dome collapses and Vulcanian explosions: Application to hazard
638 assessment in Montserrat, in: Druitt, T.H., and Kokelaar, B.P., (Eds.), The eruption of
639 Soufrière Hills Volcano, Montserrat, from 1995 to 1999: Geological Society of London
640 Memoir 21, pp. 517–537, doi:10.1144/GSL.MEM.2002.021.01.23.
641 Bonadonna, C., Folch, A., Loughlin, S., Puempel, H., 2011. Future developments in modelling
642 and monitoring of volcanic ash clouds: Outcomes from the first IAVCEI-WMO workshop
643 on Ash Dispersal Forecast and Civil Aviation. Bull. Volcanol. 74(1), 1–10,
644 doi:10.1007/s00445-011-0508-6.
645 Bonadonna, C., Costa, A., 2012. Estimating the volume of tephra deposits: A new simple
646 strategy. Geology 40(5), 415–418, doi:10.1130/G32769.1.
647 Bonadonna, C., Costa, A., 2013. Plume height, volume, and classification of explosive volcanic
648 eruptions based on the Weibull function. Bull. Volcanol. 75(8), 1–19, doi:10.1007/s00445-
649 013-0742-1.
650 Bonadonna, C., Costa, A., Folch, A., Koyaguchi, T, 2015. Tephra Dispersal and Sedimentation.
651 *In*: Sigurdsson, H., Houghton, B., McNutt, S., Rymer, H., Stix, J. (Eds.), The Encyclopedia
652 of Volcanoes, Elsevier Science, pp. 587–597, http://dx.doi.org/10.1016/B978-0-12-
653 385938-9.00033-X.

654 Branney, M.J., 1991. Eruption and depositional facies of the Whorneyside Tuff Formation,
655 English Lake District: an exceptionally large-magnitude phreatoplinian eruption. Geol.
656 Soc. Am. Bull. 103, 886–897.
657 Bush, J.W.M., Therber, B.A., Blanchette, F., 2003. Particle clouds in homogeneous and
658 stratified environments. J. Fluid Mech. 489, 29–54, doi:10.1017/S0022112003005160
659 Carazzo, G., Jellinek, A. M., 2012. A new view of the dynamics, stability and longevity of
660 volcanic clouds. Earth Planet. Sci. Lett. 325–326, 39–51.
661 Carazzo, G., Jellinek, A. M., 2013. Particle sedimentation and diffusive convection in volcanic
662 ash-clouds. J. Geophys. Res. 118(4), 1420–1437, doi:10.1002/jgrb.50155.
663 Chevalier, L., Donnadieu, F., 2015. Considerations on ejection velocity estimation from
664 infrared radiometer data: a case study at Stromboli volcano. J. Volcanol. Geotherm. Res.
665 302, 130–140, doi:10.1016/j.jvolgeores.2015.06.022.
666 Costa, A., Macedonio, G., Folch, A., 2006. A three-dimensional Eulerian model for transport
667 and deposition of volcanic ashes. Earth Planet. Sci. Lett. 241, 634–647,
668 doi:10.1016/j.epsl.2005.11.019.
669 Costa, A., Folch, A., Macedonio, G., 2010. A model for wet aggregation of ash particles in
670 volcanic plumes: Implications for tephra dispersion models, J. Geophys. Res. B: Solid
671 Earth 115, B09201, doi:10.1029/2009JB007175.
672 Delanoë, J., Protat, A., Vinson, J.P., Brett, W., Caudoux, C., Bertrand, F., Parent du Chatelet,
673 J., Hallali, R., Barthes, L., Haeffelin, M., Dupont, J.C., 2016. BASTA: A 95-GHz FMCW
674 Doppler Radar for Cloud and Fog Studies. J. Atmos. Ocean. Technol. 33, 1023–1037, doi:
675 10.1175/JTECH-D-15-0104.1.
676 Del Bello, E., Taddeucci, J., Michieli Vitturi, M., Scarlato, P., Andronico, D., Scollo, S.,
677 Kueppers, U., Ricci, T., 2017. Effect of particle volume fraction on the settling velocity of

volcanic ash particles: insights from joint experimental and numerical simulations. Sci. Reports 7:39620, doi:10.1038/srep39620.

Donnadieu, F., 2012. Volcanological applications of Doppler radars: A review and examples from a transportable pulse radar in L-Band, in: Bech, J., and Chau, J.L., (Eds.), Doppler Radar Observations: Weather Radar, Wind Profiler, Ionospheric Radar, and Other Advanced Applications: Intech, ISBN 979–953–307–352–0, doi:10.5772/35940.

Durant A.J., Rose, W.I., Sarna-Wojcicki, A.M., Carey, S., Volentik, A.C.M., 2009. Hydrometeor-enhanced tephra sedimentation: Constraints from the 18 May 1980 eruption of Mount St. Helens. J. Geophys. Res. 114, B03204, doi:10.1029/2008JB005756.

Ernst, G.G.J, Davis, J.P., Sparks, R.S.J., 1994. Bifurcation of volcanic plumes in a crosswind. Bull. Volcanol. 56, 159–169.

Folch, A., 2012. A review of tephra transport and dispersal models: Evolution, current status, and future perspectives. J. Volcanol. Geotherm. Res. 235-236, 96–115, doi:10.1016/j.jvolgeores.2012.05.020.

Folch, A., Costa, A., Macedonio, G., 2016. FPLUME-1.0: An integral volcanic plume model accounting for ash aggregation. Geoschi. Model Dev. 9, 431–450, doi :10.5194/gmd-9-431-2016.

Freret-Lorgeril V., Donnadieu, F., Eychenne, J., Soriaux, C., Latchimy, T., 2019. *In situ* terminal settling velocity measurements at Stromboli: input from physical characterization of ash. J. Volcanol. Geotherm. Res. 374, 62–79, https://doi.org/10.1016/j.jvolgeores.2019.02.005.

Ganser, G.H., 1993. A rational approach to drag predictionof spherical and non-spherical particles. Powder Technol. 77, 143–152, doi:10.1016 /0032-5910(93)80051-B.

Gouhier, M., Donnadieu, F., 2008. Mass estimations of ejecta from Strombolian explosions by inversion of Doppler radar measurements. J. Geophys. Res. 113(10), 1–17. doi:10.1029/2007JB005383.

Hobbs, P.V., Radke, L.F., Lyons, J.H., Ferek, R.J., Coffman, D.J., 1991. Airborne measurements of particle and gas emissions from the 1990 volcanic eruptions of Mount Redoubt. J. Geophys. Res. 96, 18,735–18,752.

Horwell C.J., Baxter P.J., 2006. The respiratory health hazards of volcanic ash: a review for volcanic risk mitigation. Bull. Volcanol. 69(1), 1–24, doi:10.1007/s00445-006-0052-y.

Hoyal, D.C.J.D., Bursik, M.I., Atkinson, J.F., 1999. Settling-driven convection: A mechanism of sedimentation from stratified fluids. J. Geophys. Res. 104, 7953–7966, doi:10.1029/1998JC900065.

Kozono, T., Iguchi, M., Miwa, T, Maki, M., Maesaka, T., Miki, D., 2019. Characteristics of tephra fall from eruptions at Sakurajima volcano, revealed by optical disdrometer measurements. Bull. Volcanol. 81:41, doi:10.1007/s00445-019-1300-2.

Löffler-Mang, M., Jürg, J., 2000. An Optical Disdrometer for Measuring Size and Velocity of Hydrometeors. J. Atmos. Ocean. Technol. 17, 130–139.

Manzella, I., Bonadonna, C., Phillips, J.C., Monnard, H., 2015. The role of gravitational instabilities in deposition of volcanic ash. Geology 43, 211–214, doi:10.1130/G36252.1.

Mastin, L.G., Guffanti, M., Servranckx, R., Webley, P., Barsotti, S., Dean, K., Durant, A., Ewert, J.W., Neri, A., Rose, W.I., Schneider, D., Siebert, L., Stender, B., Swanson, G., Tupper, A., Volentik, A., Waythomas, C.F., 2009. A multidisciplinary effort to assign realistic source parameters to models of volcanic ash-cloud transport and dispersion during eruptions. J. Volcanol. Geotherm. Res. 186, 10–21, doi:10.1016/j.volgeores.2009.01.008.

Montopoli, M., 2016. Velocity profiles inside volcanic clouds from three-dimensional scanning microwave dual-polarization Doppler radars. J. Geophys. Res. Atmos. 121, 7881-7900, doi:10.1002/2015JD023464.

Patrick, M.R., Harris, A.J.L., Ripepe, M., Dehn, J., Rothery, D.A., Calvari, S., 2007. Strombolian explosive styles and source conditions: Insights from thermal (FLIR) video. Bull. Volcanol. 69(7), 769–784, doi:10.1007/s00445-006-0107-0.

Pfeiffer, T., Costa, A., Macedonio, G., 2005. A model for the numerical simulation of tephra fall deposits. J. Volcanol. Geotherm. Res. 140, 273–294, doi:10.1016/j.volgeores.2004.09.001.

Ripepe, M., Rossi, M., Saccorotti, G., 1993. Image processing of explosive activity at Stromboli. J. Volcanol. Geotherm. Res. 54(3-4), 335–351, doi:10.1016/0377-0273(93)90071.

Sauvageot, H., 1992. *Radar meteorology*, Artech House, ISBN 0890063184, Boston.

Scharff, L., Hort, M., Varley, N.R., 2015. Pulsed Vulcanian explosions: A characterization of eruption dynamics using Doppler radar. Geology 43(11):G36705.1.

Scollo, S., Prestifilippo, M., Spata, G., D'Agostino, M. & Coltelli, M., 2009. Monitoring and forecasting Etna volcanic plumes. Nat. Hazard. Earth Sys. Sci. 9, 1573–1585.

Scollo, S., Prestifilippo, M., Coltelli, M., Peterson, R.A. & Spata, G., 2010. A statistical approach to evaluate the tephra deposit and ash concentration from PUFF model forecasts. J. Volcanol. Geotherm. Res. 200, 129–142, doi:10.1016/j.volgeores.2010.12.004.

Scollo, S., Coltelli, M., Bonadonna, C., Del Carlo, P., 2013. Tephra hazard assessment at Mt. Etna (Italy). Nat. Hazard. Earth Sys. Sci. 13, 3221–3233, doi:10.5194/nhess–13–3221–2013.

747 Scollo, S., Bonadonna, C., Manzella, I., 2017. Settling-driven gravitational instabilities
748 associated with volcanic clouds: new insights from experimental investigations. Bull.
749 Volcanol. 79:39, doi:10.1007/s00445-017-1124-x.
750 Suzuki, Y.J., Koyaguchi, T., 2013. 3D numerical simulation of volcanic eruption clouds during
751 the 2011 Shinmoe-dake eruptions. Earth Planet. Space 65, 581–589,
752 doi:10.5047/eps.2013.03.009.
753 Tokay, A., Wolff, D.B., Petersen, W.A., 2014. Evaluation oft he New Version of the Laser-
754 Optical Disdrometer, OTT Parsivel^2. J. Atmos. Ocean. Tech. 31, 1276–1288,
755 doi:10.1178/JTECH-D-13-00174.1.
756 Turner, J.S., 1960. A comparison between buoyant vortex rings and vortex pairs. J. Fluid Mech.
757 7(3), 419–432, https://doi.org/10.1017/S0022112060000189.
758 Wilson, T.M., Stewart, C., Sword-Daniels, V., Leonard, G.S., Johnston, D.M., Cole, J.W.,
759 Wardman, J., Wilson, G., Barnard, T.S., 2012. Volcanic ash impacts on critical
760 infrastructure. Phys. Chem. Earth 45-46, 5–23, https://doi.org/10.1016/j.pce.2011.06.006.